A Non-axisymmetric E×B Shear Inducing Toroidally Localized Turbulence with applied Magnetic Perturbation Field in EAST

G. H. Hu[1], R. Chen[1*], G. S. Xu[1*], H. Y. Guo[2], Y. W. Sun[1], Y. F. Liang[1,3], J. L. Xie[4], C. Zhou[4], X. L. Jin[4], S. Gu[1], M. N. Jia[1], Y. F. Wang[1], L. Wang[1], J. C. Xu[1], Q. Q. Yang[1], S. C. Liu[1], X. Q. Wu[1], T. Zhang[1], Q. Zang[1], L. Chen[1], N. Yan[1], L. M. Shao[1], Y. Ye[1], S. Y. Ding[1], B. N. Wan[1], and EAST Team

[1]Institute of Plasma Physics, Chinese Academy of Sciences, Hefei 230031, China

[2]General Atomics, P.O. Box 85608, San Diego, California 92186-5608, USA

[3]Institute for Energy and Climate Research-Plasma Physics, Forschungszentrum Jülich, Association EURATOM-FZJ, Trilateral Euregio Cluster, 52425 Jülich, Germany

[4]University of Science and Technology of China, Hefei 230026, China

*Corresponding author. chenran@ipp.ac.cn, gsxu@ipp.ac.cn

Abstract

The local **E×B** shear has been demonstrated to be correlate with controlling 3D structure of turbulence in the edge transport barrier (pedestal) on the EAST superconducting tokamak with edge localized modes (ELMs) suppressed by externally applied 3D magnetic fields. The toroidal variations of turbulence intensity, spectrum width and eddy tilting are found to be correlated with the local **E×B** shear, may thus providing the potential mechanism for 3D-field-induced nonaxisymmetric **E×B** shear in regulating the turbulence. These new findings may significantly advance the understanding of pedestal transport and structure with applied 3D fields for ELM control, which is critical for next-step fusion development.

Keywords: resonant magnetic perturbation, turbulence, pedestal, edge localized mode

1. Introduction

A crucial issue for a fusion reactor is transient heat and particle fluxes caused by large-size edge-localized modes (ELMs). ELMs can significantly reduce the lifetime of plasma facing components (PFCs) due to erosion at their surface [1]. This poses an increased fundamental scientific challedge for next-step fusion develop. Thus, ELM control is believed to be critically important to magnetic fusion research.

Applying resonant magnetic perturbation (RMP) is one of the promising techniques utilized to control ELMs [2]. This method has been proven to be successful in either suppressing the ELMs in EAST [3, 4], DIII-D [5] and KSTAR [6], or in the mitigating the ELM power in JET [7], ASDEX-U [8] and MAST [9]. ELMs suppression has well-established as a resonant effect which requires certain circumstances [10]. However, previous experimental results suggest that the achievement of ELMs suppression is generally accompanied by a significant reduction of plasma density ('density pumpout') [11]. Density pump out is widely believed that it is induced by the increase of plasma transport [12]. Turbulence transport is often thought to be one of the main transport mechanisms in tokamak. Turbulence suppression and associated transport reduction by **E×B** shear play a central role in magnetic fusion and other laboratory systems for the formation of transport barriers and enhancement of plasma confinement [13-15]. Understanding the 3D interaction between the turbulence and **E×B** shear is thus the key to uncover the physics behind the ELM control.

Experiments in the DIII-D tokamak indicated that, when ELMs are suppressed, the ion-scale turbulence increases rapidly and significantly in pedestal region [16]. The toroidally localized increase in fluctuation intensity is concomitant with a slight increase in the local density gradient [17]. In the AUG tokamak, field-line localized ballooning modes were observed in the pedestal of an ELMy H-mode plasma, attributed to a 3D distortion of the local magnetic shear [18]. In addition, it was reported in AUG that the application of RMPs to L-mode plasmas leads to a nonaxisymmetric modification to the edge turbulence as well as the radial electric field E_r, which appears to be sensitive to the resonance degree of RMPs, possibly dependent on the plasma

response to RMPs [19]. In H-mode discharges, the scrape-off layer (SOL) cross-field transport rise is observed when ELMs are mitigated [20]. In KSTAR, the strong nonlinear coupling between turbulence and ELMs are clearly observed, this implies that the exchange of energy between them may be helpful to prevent large scale crashes [21, 22]. The small scale turbulence also can be modified by 3D fields in RFX-mode device, the modification is deeply connected to the variation of turbulence induced particle transport [23]. In the vicinity of SOL region, the formation of island like structure may correlates with edge plasma potential [24] and pressure [25], consequently affects the fluctuation behaviors.

This paper provides experimental evidence that the 3D-field-induced non-axisymmetric **E×B** shear can become a possible mechanism for the formation of 3D turbulence structure in a toroidal plasma with successful ELM suppression by applied 3D fields without any detectable density pumpout. These results are recently obtained from EAST for long pulse operation, where a rotating RMP is applied to realize a toroidal scan of its induced magnetic footprints and the consequent heat and particle fluxes on divertor targets. EAST is equipped with various radially-resolved diagnostics for edge profile and fluctuation measurements. Radial profiles of electron density and temperature are measured by microwave reflectometry [26] and Thomson scattering (TS) [27] systems separately. The diagnostics employed for turbulence measurement are the lithium beam spectroscopy (Li-BES) [28], electron cyclotron emission imaging (ECEI) [29] and Doppler backscattering (DBS) [30]. Meanwhile, the flexible 3D coil system which can generate toroidally rotatable magnetic perturbations [31]. Thus, these advantages provide the unique capacity for comprehensive characterizations of both fluctuation structure and the **E×B** shear. The toroidal variations of fluctuation spectra, eddy tilting and radial location displacement, as well as fluctuation intensity, have been observed in the pedestal of H-mode plasmas when RMPs are applied to suppress ELMs. Furthermore, the changes of toroidally localized fluctuations appear to strongly correlate with the local **E×B** shear rather than the local electron density/pressure gradient or local magnetic shear.

2. Results

In this study, an n = 1 RMP rotating slowly in the toroidal direction at 0.5 Hz is applied to an upper single null H-mode plasma, heated by radio-frequency waves at 4 MW, with toroidal field B_T = 2.45 T, plasma current I_p = 450 kA, normalized beta β_N = 1, edge safety factor q_{95} = 6, plasma elongation factor κ = 1.7 and triangularity δ = 0.47. The normalized electron collisionality at the pedestal top is ν_{*e} = 1.4. ELMs are mostly suppressed during the RMP phase from t = 3 to 7 s, except a short period near t = 4.9 s when ELMs reappear due to an impurity event, as indicated by the divertor D_α emission in figure 1(b). The maximum changes in the central line-averaged electron density $\bar{n}_e$ and the energy confinement improvement factor H_{98} are both within 5%. The pedestal top electron density $n_{e,ped}$ from reflectometer at around Ψ_p = 0.9 is given in figure 1(d). The maximum variation of $n_{e,ped}$ is less than 8% which agree with $\bar{n}_e$ change. The above observations indicate that no obvious RMP-induced density pumpout or associated deterioration of the global energy confinement. Prior to RMP switch-on, the fluctuations in the pedestal are dominated by an edge coherent mode (ECM) [32, 33] at a frequency of ~ 25 kHz, as illustrated by the spectrograms in figure 2, measured at the low-field-side midplane by the Li-BES and ECEI. The ECM is a high-n electrostatic mode, which has been identified as the dissipative trapped electron mode, frequently appearing in the H-mode pedestal at high collisionality in EAST. This mode is driven by steep pressure gradient and localized radially in the steep-pressure-gradient region. It can drive significant particle and heat transport, contributing to ELM suppression [32]. With the toroidal rotation of the RMP fields, the toroidal-angle distribution of the fluctuations can be measured at a fixed toroidal location as a time-dependent periodic evolution.

The application of RMPs results in a remarkable change in the ECM-dominated pedestal fluctuations. The spectrograms in figure 2 exhibit strong n = 1 toroidal

variations. The ECM evolves from an axisymmetric coherent mode before the application of RMPs into nonaxisymmetric broadband fluctuations, which vary continuously in the toroidal direction from enhanced intensity and significantly broadened spectrum at one toroidal location to deep suppression at the opposite toroidal location. Both the Li-BES and ECEI measurements show that the maximum spectral intensity and bandwidth of the pedestal fluctuations shift radially between two adjacent channels, i.e., R = 2.313 m in (a) and R = 2.297 m in (b) for Li-BES; R = 2.325 m in (c) and R = 2.307 m in (d) for ECEI. The direction of the shift is consistent with the 3D radial displacement of the magnetic flux surface at that toroidal location induced by the n = 1 RMPs based on the linear MHD modeling code MARS-F [34] calculations [see figure 3(c)].

To elucidate the relationship between the toroidal variations in the RMP-induced nonaxisymmetric fluctuation intensity and the changes in the local density profile in the pedestal, figure 3 shows the temporal evolutions of pedestal fluctuation intensities for the radial channel with the highest fluctuation intensity (usually near the radial location of pressure gradient peak) measured by the Li-BES, ECEI and DBS, along with the normalized inverse density gradient scale length ($a / L_{n_e} = a\nabla n_e / n_e$) and the radial displacement of peak density gradient location in figure 3(c), measured by a reflectometer. Figure 3(e) depicts the layout of the diagnostics for the pedestal fluctuation and profile measurements, with their toroidal angles relative to the first RMP coil (U1 or L1) also indicated. All three fluctuation diagnostics, i.e., Li-BES, ECEI and DBS, show a periodic evolution of the pedestal fluctuation intensity following the toroidal rotation of the RMPs. The time shifts, i.e., the toroidal angle differences, between the fluctuation intensity peaks detected by the three fluctuation diagnostics agree very well with respect to their different toroidal locations. Moreover, a toroidally varying radial displacement up to ± 0.7 cm (± 1.5 % of the minor radius) in the pedestal electron density profile is detected which agrees well with MARS-F prediction, as shown in figure 3(c). Such an RMP-induced radial displacement has been observed in several devices [35]. Figure 3 indicates that the pedestal fluctuation

intensity peaks as the local density profile shifts to the outermost location, and is strongly reduced as the local density profile shifts to the innermost location. Note that the increase in the pedestal fluctuation intensity is correlated with a reduction in the local normalized inverse density gradient scale length, in contrast the previous results from DIII-D [17].

To further illustrate the correlation between the RMP-induced nonaxisymmetric pedestal fluctuations with the local profiles, figure 4 shows the radial profiles of electron density, temperature, pressure and their radial gradients for three typical moments, i.e., before the application of RMPs, at the highest fluctuation level (and also with the broadest spectrum) during the application of RMPs and after fluctuations being deeply suppressed by RMPs. These results further confirm a 3D distortion of the edge profiles induced by RMPs, which appears to be more significant in the electron density profiles than the temperature profiles, consistent with the previous observations [35]. The toroidal variations of pedestal fluctuation intensity appear to be anti-correlated with those of the local radial gradients. Compared with the case before the application of RMPs, the pedestal fluctuation intensity doubles [see figure 3(b)] for the case at the highest fluctuation level, while, in this case, the maximum local radial gradients in pedestal electron pressure ∇p_e, density ∇n_e and temperature ∇T_e all decrease. Hence, this indicates that the enhanced pedestal fluctuations are not driven by the local radial gradient forces. For the case with deeply suppressed fluctuations, the fluctuation intensity is reduced by ~80% with respect to the case without RMPs. However, the maximum ∇p_e and ∇n_e actually increase by ~10%. Thus, these experimental results clearly rule out the change in the local electron density/pressure gradients as a mechanism underlying the toroidal variation of pedestal fluctuation intensity.

We have also examined the toroidal variation of local magnetic shear as a possible mechanism regulating the pedestal fluctuations [18, 36]. The local magnetic shear usually maximizes or minimizes at the zero-crossing point of the radial displacement of magnetic flux surfaces [18]. However, neither the maximum nor the minimum in the pedestal fluctuation intensity appears near the zero-crossing point, i.e., the

maximum/minimum fluctuation intensity does not appear at the toroidal locations where the local magnetic shear minimizes/maximizes, thus ruling out the possibility of 3D distortion of local magnetic shear as a driving mechanism.

In contrast to the previous findings, the toroidal variation of the pedestal fluctuation intensity, as observed in EAST, appear to be associated with the change in the local $\mathbf{E_r}\times\mathbf{B}$ shear. Figure 5 compares the temporal evolutions of (a) the pedestal fluctuation intensity and (b) the radial electric field gradient $|\nabla E_r|$, both measured by DBS, as well as (c) a/L_{n_e} measured by reflectometer during the toroidal rotation of n = 1 RMPs, together with the density contour in the pedestal. The radial displacements of the density contour lines and a/L_{n_e} peaks are largely consistent with the displacement of the magnetic flux surfaces [18]. The black circles (before the application of RMPs), blue squares (at the highest fluctuation level with RMPs) and purple diamonds (after fluctuations being deeply suppressed by RMPs) in (b) and (c) mark the radial locations of fluctuation intensity peaks, as determined from the Li-BES measurements. As can be seen, the radial locations of the pedestal fluctuation intensity peaks are always very close to the a/L_{n_e} peaks and follow the toroidally varying radial displacements of the density profiles or the 3D distortion of the magnetic flux surfaces. This evolution agrees with previous research result where ECM is driven by the local density or pressure gradient [33]. Furthermore, the pedestal fluctuation intensity maximizes when its radial peak and the a/L_{n_e} peak shift radially to the outermost location at $R \sim 2.313$ m where both a/L_{n_e} and $|\nabla E_r|$ are small; while it minimizes when its radial peak and the a/L_{n_e} peak shift radially to the innermost location at $R \sim 2.297$ m where both a/L_{n_e} and $|\nabla E_r|$ are large. It appears that the toroidal variations of the pedestal fluctuation intensity are inversely correlated with the local $\mathbf{E_r}\times\mathbf{B}$ shear, as well as the local density gradient. Thus, the toroidal variations in the pedestal fluctuation intensity during the application of RMPs may be induced by the toroidally localized $\mathbf{E_r}\times\mathbf{B}$ shear suppression. Recent experiments in DIII-D, RMP coil current is flipped rapidly [17].

Broadband turbulence formation is concomitant with an increase in the density gradient, suggesting that the pressure gradient increase could be a mechanism for turbulence increase. To better show the detailed evolutions of fluctuation bandwidth broadening and pedestal structure, a slow rotating n=1 RMP is applied in our experiment. As we can see in figure 5, the driven mechanism is obviously different with DIII-D result.

To further demonstrate the radial correlation between the fluctuation intensity and the local $\mathbf{E_r}\times\mathbf{B}$ shear, figure 6 shows the radial profiles of the density fluctuation intensity measured by Li-BES, the radial electric field E_r measured by DBS and the local $\mathbf{E_r}\times\mathbf{B}$ shearing rate, $\Omega_{E_r\times B}=\left|RB_{pol}B_T^{-1}\,\partial E_r/\partial(RB_{pol})\right|$ estimated from E_r, for the above-mentioned three cases. A toroidally varying E_r -well structure appears in the pedestal, which moves radially, together with the radial displacement of the pedestal fluctuation intensity peak. When the E_r well, the fluctuation intensity peak and the density profile [figure 4(a)] shift to the outermost location, the E_r well becomes shallower with reduced $\left|E_r\right|$ at the valley point relative to the pre-RMP case. On the contrary, when the E_r well, the fluctuation intensity peak and the density profile shift to the innermost location, the E_r well becomes deeper relative to the pre-RMP case. The local shearing rate decreases/increases from $0.4\times10^6\ \mathrm{s}^{-1}$ in the pre-RMP case to $0.27\times10^6\ \mathrm{s}^{-1}$ (32% lower) in the highest fluctuation level case or $0.55\times10^6\ \mathrm{s}^{-1}$ (38% higher) in the deeply suppressed fluctuation case. As the pedestal fluctuation intensity increases/decreases, the fluctuation spectrum becomes significantly broadened/suppressed, which is consistent with the physical picture of toroidally localized fluctuation suppression via the well-known $\mathbf{E_r}\times\mathbf{B}$ shear decorrelation effect [13, 37]. In addition, the edge n_e and T_e profiles can be used to estimate diamagnetic term contribution to E_r [38]. From the previous experimental results [4], one may consider that pedestal electron temperatures and ion temperatures are roughly similar. By invoking quasi-neutrality, the measured effective charge Z_{eff}=2.3 on the ion density

is taken into account. As shown in Figure 6(c), the toroidal variation of E_r is positively correlated with that of the local diamagnetic term.

Additional evidence for the critical role of local $\mathbf{E_r}\times\mathbf{B}$ shear in regulating the pedestal fluctuations comes from ECEI pedestal fluctuation imaging, as shown in figures. 6 (e)-(g). With enhanced local $\mathbf{E_r}\times\mathbf{B}$ shear, the fluctuation eddies appear to be strongly tilted and moves to the innermost location relative to the magnetic separatrix reconstructed from EFIT [figure 6(g)]. The tilting direction is well consistent with that of the local $\mathbf{E_r}\times\mathbf{B}$ shear. On the contrary, the fluctuation eddies appear to be weakly tilted and move to the outermost location [figure 6(f)] as the local $\mathbf{E_r}\times\mathbf{B}$ shear is reduced. The ratio of radial to poloidal wavenumber spectral bandwidth $\Delta k_r / \Delta k_\theta$ can be used to depicts turbulent eddy shape [39]. Using radially and poloidally spaced ECEI channels, the radial (poloidal) fluctuation spectral density *S(k, f)* and power-averaged dispersion $\bar{k}_f$ are obtained by the standard two-point cross-correlation technique [39]. Radial and poloidal wavenumber spectral bandwidth are calculated by $\triangle k = \left(\sum_{k,f} S(k,f) \cdot [k - \bar{k}_f]^2 / \sum_{k,f} S(k,f) \right)^{1/2}$. Here $\bar{k}_f = \sum_k k \cdot S(k,f) / S(f)$ and *S(f)* is the frequency spectral. Analysis is based on time window of 512 μs containing 512 data points and 16 000 data points in total are used for this calculation. The time window has an overlap of 256 time points. The $\Delta k_r / \Delta k_\theta$ increases from 0.22 in the pre-RMP case to 0.48 (more tilted) in the deeply suppressed fluctuation case, but decreases to 0.09 (less tilted) in the highest fluctuation case. These observations provide further support for the local $\mathbf{E_r}\times\mathbf{B}$ shear as the primary mechanism in regulating the pedestal fluctuations with applied 3D fields.

3. Summary

In summary, the EAST experiments demonstrate the local $\mathbf{E}\times\mathbf{B}$ shear as a possible physics mechanism regulating the 3D pedestal fluctuations with the application of RMPs. This is evidenced by the strong toroidal correlation between the local $\mathbf{E}\times\mathbf{B}$ shear

and the local spectral bandwidth broadening, eddy tilting as well as intensity changes of pedestal fluctuations. Furthermore, the results exclude the possibility of the RMP-induced modifications to either local electron density/pressure gradient or local magnetic shear as a driving mechanism in these experimental conditions. We found that RMP can suppress ELMs even without introducing either a density pumpout or any noticeable global changes of other parameters in contrast to previous observations [2, 3, 6, 7]. This implies that, in this case, rather than the formation of a stochastic boundary layer [2, 40], the RMP-induced 3D pedestal structure may play a key role in suppressing ELMs. These new findings may shed further light on understanding the critical role of 3D fields on ELM control for long pulse operation.

Acknowledgements

This work is supported by the National Natural Science Foundation of China under Grants No. 11705235, No. 11875294, No. 11575235 and No. 11575236, and the National Magnetic Confinement Fusion Science Program of China under Grants No. 2015 GB101000.

References

[1] Loarte A. *et al.* 2013 *Nucl. Fusion* **53** 083031.

[2] Evans T.E. *et al.* 2006 *Nature Physics* **2** 419-423.

[3] Sun Y. *et al.* 2016 *Phys. Rev. Lett.* **117** 115001.

[4] Sun Y. *et al.* 2017 *Nucl. Fusion* **57** 036007.

[5] Wade M.R. *et al.* 2015 *Nucl. Fusion* **55** 023002.

[6] Park J.-K. *et al.* 2018 *Nature Physics* **14** 1223-1228.

[7] Liang Y. *et al.* 2007 *Phys. Rev. Lett.* **98** 265004.

[8] Suttrop W. *et al.* 2011 *Phys. Rev. Lett.* **106** 225004.

[9] Kirk A. *et al.* 2010 *Nucl. Fusion* **50** 034008.

[10] Suttrop W. *et al.* 2018 *Nucl. Fusion* **58** 096031.

[11] Evans T.E. *et al.* 2008 *Nucl. Fusion* **48** 024002.

[12] Taimourzadeh S., Shi L., Lin Z., Nazikian R., Holod I. and Spong D. 2019 *Nucl.*

Fusion **59** 046005.

[13] Burrell K.H. 1997 *Phys. Plasmas* **4** 1499-1518.

[14] Castejón F. *et al.* 2017 *Nucl. Fusion* **57** 102022.

[15] Schaffner D.A., Carter T.A., Rossi G.D., Guice D.S., Maggs J.E., Vincena S. and Friedman B. 2012 *Phys. Rev. Lett.* **109** 135002.

[16] McKee G.R. *et al.* 2013 *Nucl. Fusion* **53** 113011.

[17] Wilcox R.S. *et al.* 2016 *Phys. Rev. Lett.* **117** 135001.

[18] Willensdorfer M. *et al.* 2017 *Phys. Rev. Lett.* **119** 085002.

[19] Conway G.D., Fietz S., Müller H.W., Lunt T., Simon P., Suttrop W., Maraschek M., Happel T. and Viezzer E. 2015 *Plasma Phys. Controlled Fusion* **57** 014035.

[20] Müller H.W. *et al.* 2013 *J. Nucl. Mater* **438** S64-S71.

[21] Lee J. *et al.* 2019 *Nucl. Fusion* **59** 066033.

[22] Lee J., Yun G.S., Choi M.J., Kwon J.M., Jeon Y.M., Lee W., Luhmann N.C. and Park H.K. 2016 *Phys. Rev. Lett.* **117** 075001.

[23] Vianello N. *et al.* 2015 *Plasma Phys. Controlled Fusion* **57** 014027.

[24] Ciaccio G., Schmitz O., Spizzo G., Abdullaev S.S., Evans T.E., Frerichs H. and White R.B. 2015 *Phys. Plasmas* **22** 102516.

[25] Xu Y. *et al.* 2007 *Nucl. Fusion* **47** 1696.

[26] Qu H. *et al*. 2015 *Plasma Sci. Technol.* **17** 985.

[27] Zang Q. *et al* 2016 *Nucl. Fusion* **56** 106003.

[28] Zoletnik S. *et al.* 2018 *Rev. Sci. Instrum.* **89** 063503.

[29] Gao B.X. *et al.* 2018 *J. Instrum.* **13** P02009.

[30] Zhou C. *et al.* 2013 *Rev. Sci. Instrum.* **84** 103511.

[31] Sun Y., Liang Y., Qian J., Shen B. and Wan B. 2015 *Plasma Phys. Controlled Fusion* **57** 045003.

[32] Wang H.Q. *et al.* 2014 *Phys. Rev. Lett.* **112** 185004.

[33] Ye Y. *et al.* 2017 *Nucl. Fusion* **57** 086041.

[34] Liu Y., Kirk A., Gribov Y., Gryaznevich M.P., Hender T.C. and Nardon E. 2011 *Nucl. Fusion* **51** 083002.

[35] Chapman I.T. *et al.* 2014 *Nucl. Fusion* **54** 083006.

[36] Hegna T.M.B.a.C.C. 2013 *Nucl. Fusion* **53** 013004.

[37] Biglari H., Diamond P.H. and Terry P.W. 1990 *Physics of Fluids B: Plasma Physics* **2** 1-4.

[38] McDermott R.M. *et al.* 2009 *Phys. Plasmas* **16** 056103.

[39] Beall J.M., Kim Y.C. and Powers E.J. 1982 *J. Appl. Phys.* **53** 3933.

[40] Schmitz O. *et al.* 2009 *Phys. Rev. Lett.* **103** 165005.

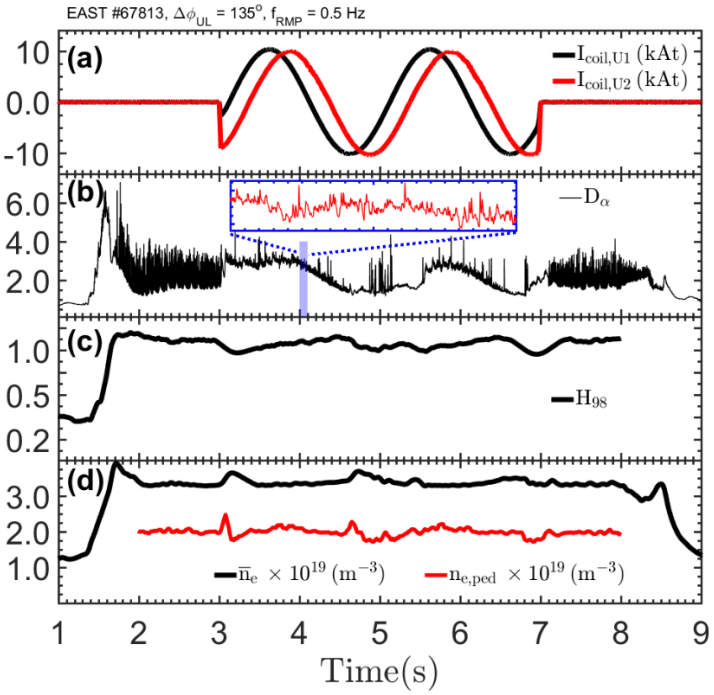

Figure. 1 (color online). Time traces of (a) RMP coil currents, (b) divertor D_α emission, (c) energy confinement improvement factor H_{98}, (d) central line-averaged electron density $\bar{n}_e$ and pedestal top electron density $n_{e,ped}$ at around $\Psi_p = 0.9$. The spikes in $\bar{n}_e$ near t = 3.1 and 4.9 s are caused by impurity events. The n = 1 RMPs with a fixed poloidal spectrum rotates toroidally from t = 3 to 7 s for two cycles.

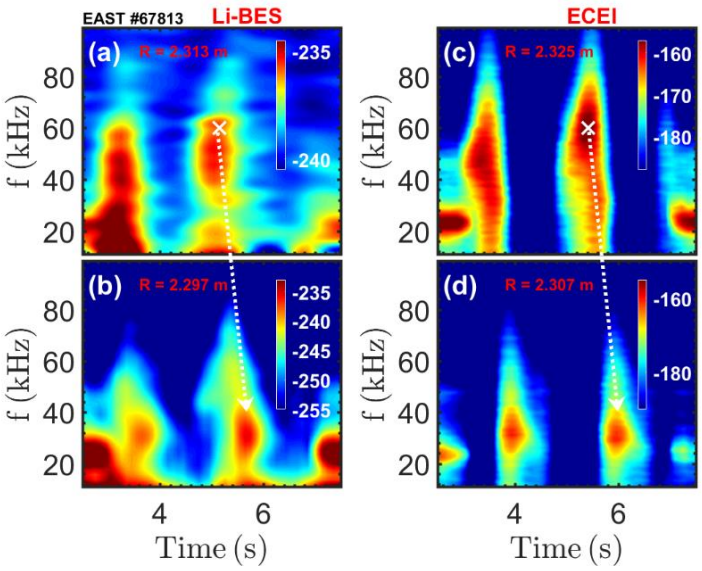

Figure. 2 (color online). Spectrograms of pedestal density fluctuation measured by Li-BES at (a) R = 2.313 m and R = 2.297 m, and ECEI at (c) R = 2.325 m and (d) R = 2.307 m. The white crosses mark the time points of the maximum fluctuation intensity as measured by Li-BES and ECEI.

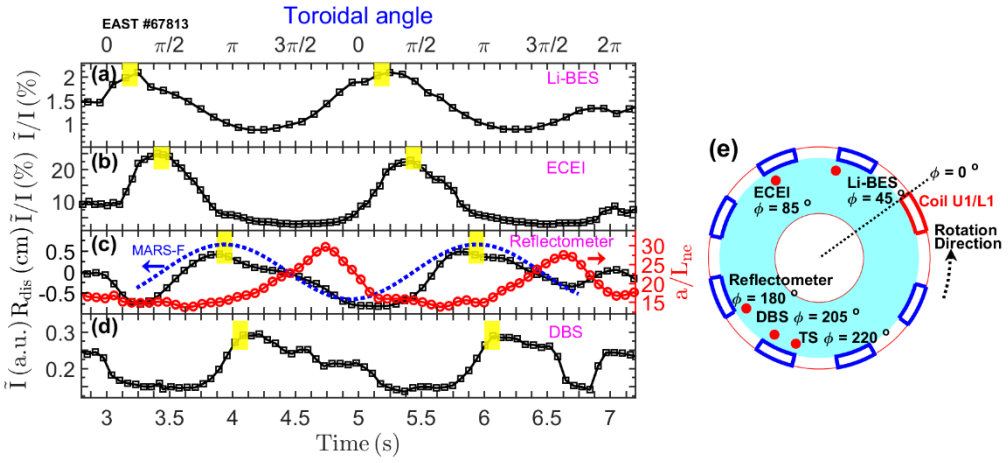

Figure. 3 (color online). Time traces of pedestal fluctuation intensities for the radial channel with the highest fluctuation intensity measured near the outer mid plane by (a) Li-BES, (b) ECEI and (d) DBS, all integrated over 10-80 kHz; (c) the temporal evolutions of normalized inverse density gradient scale length a / L_{n_e} (red, right axis), the radial displacement of density gradient region (black, left axis) provides by a reflectometer and plasma movements predicted by MARS-F (blue, left axis); (e) toroidal layout of the EAST RMP coils and involved diagnostics. Toroidal locations of

these diagnostics are also indicated in the left plot by yellow shaded areas.

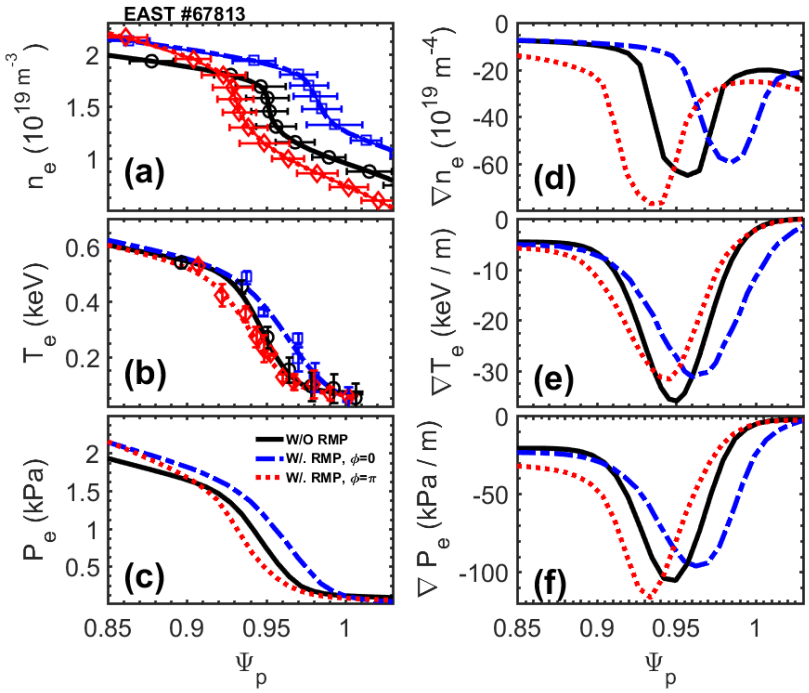

Figure.4 (color online). Comparison of edge profiles of electron (a) density, (b) temperature, (c) pressure, and their radial gradients, (d) density, (e) temperature and (f) pressure, among the three cases: before the application of RMPs (black solid line), for the highest fluctuation level during the application of RMPs (blue dashed line, $\Phi = 0$) and for fluctuations being deeply suppressed by RMPs (red dotted line, $\Phi = \pi$). All the quantities are plotted vs. the normalized poloidal magnetic flux Ψ_p.

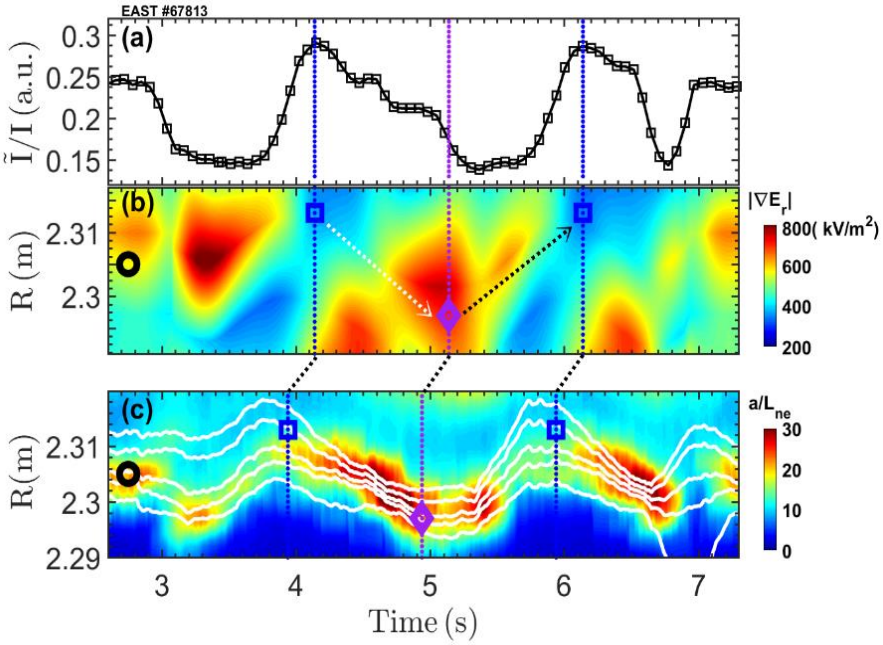

Figure. 5 (color online). Time-resolved (a) density fluctuation intensity integrated over 10-80 kHz for the radial channel with the highest fluctuation intensity and (b) the absolute value of radial electric field gradient calculated as the difference between radially adjacent channels, both measured by DBS. (c) The temporal evolution of radial distribution of normalized inverse density gradient length a / L_{n_e} measured by reflectometer, where the density contour is also displayed in white lines. Black circles (without RMPs), blue squares (for the highest fluctuation level with RMPs) and purple diamonds (for fluctuations being deeply suppressed with RMPs) in (b) and (c) mark the radial locations of fluctuation intensity peaks, determined by the Li-BES measurements. Note that the markers in (c) are shifted in time according to the relative toroidal angle between the DBS and reflectometer during the RMP application.

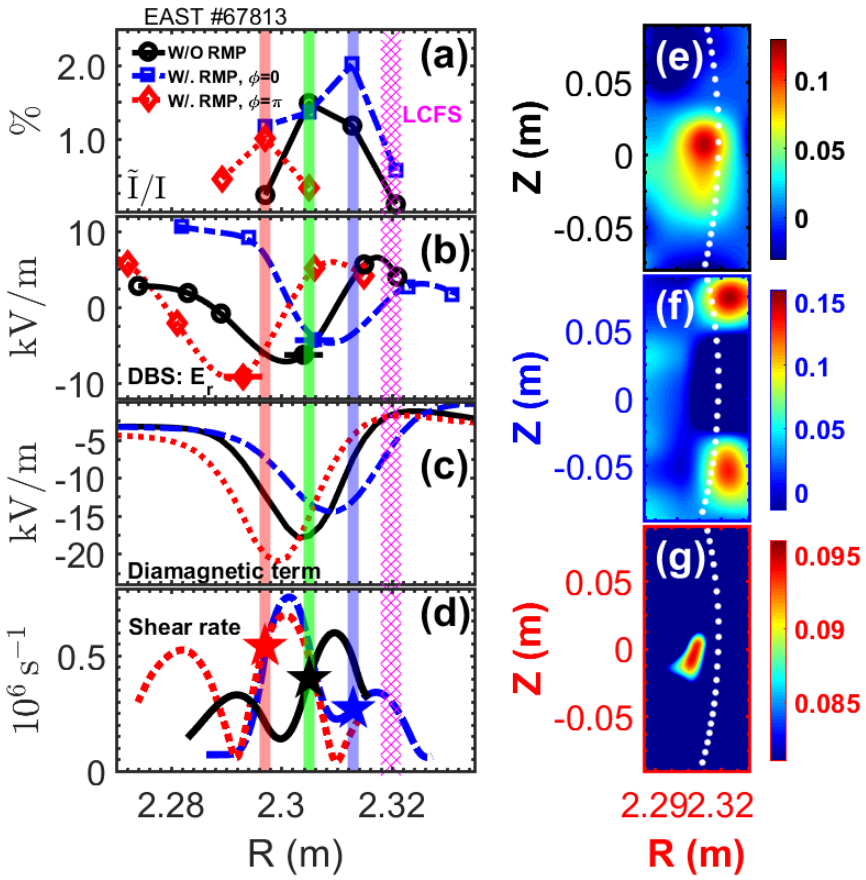

Figure. 6 (color online). Radial distributions of (a) density fluctuation intensity integrated over 10-80 kHz from Li-BES, (b) edge radial electric field from DBS, (c) an estimation of diamagnetic term contribution to E_r and (d) local $\mathbf{E_r}\times\mathbf{B}$ shearing rate estimated from (b) in the three cases: without RMPs (black solid curves), for the highest fluctuation level with RMPs (blue dashed curves, $\Phi = 0$) and for fluctuations being deeply suppressed (red dotted curves, $\Phi = \pi$) with RMPs. The vertical shaded bars together with the pentagrams in (d) highlight the radial locations of the fluctuation intensity peaks. The separatrix resides in the magenta shadow region. Snapshots of pedestal fluctuations measured by ECEI in the above-mentioned three cases are shown in (e) black, (f) blue and (g) red. The white dotted lines mark the magnetic separatrix reconstructed from EFIT.